A high-order compact local integrated-RBF scheme for steady-state incompressible viscous flows in the primitive variables

N. Thai-Quang, K. Le-Cao, N. Mai-Duy and T. Tran-Cong

Computational Engineering and Science Research Centre, Faculty of Engineering and Surveying, The University of Southern Queensland, Toowoomba, Queensland 4350, Australia.

Abstract: This study is concerned with the development of integrated radial-basis-function (IRBF) method for the simulation of two-dimensional steady-state incompressible viscous flows governed by the pressure-velocity formulation on Cartesian grids. Instead of using low-order polynomial interpolants, a high-order compact local IRBF scheme is employed to represent the convection and diffusion terms. Furthermore, an effective boundary treatment for the pressure variable, where Neumann boundary conditions are transformed into Dirichlet ones, is proposed. This transformation is based on global 1D-IRBF approximators using values of the pressure at interior nodes along a grid line and first-order derivative values of the pressure at the two extreme nodes of that grid line. The performance of the proposed scheme is investigated numerically through the solution of several linear (analytic tests including Stokes flows) and non-linear (recirculating cavity flow driven by combined shear & body forces and lid-driven cavity flow) problems. Unlike the global 1D-IRBF scheme, the proposed method leads to a sparse system matrix. Numerical results indicate that (i) the present solutions are more accurate and converge faster with grid refinement in comparison with standard finite-difference results; and (ii) the proposed boundary treatment for the pressure is more effective than conventional direct application of the Neumann boundary condition.

Keywords: viscous flow, primitive variables, Cartesian grid, integrated radial basis function, high-order approximation, compact local stencil.

1 Introduction

It is known that the equations of motion of a Newtonian fluid can be obtained via several formulations, including those based on the velocity-pressure ($\widehat{u}-p$), the stream function-vorticity ($\psi-\omega$) and the stream function (ψ) variables. The last two involve less dependent variables than the first one. However, they require some special treatments for the handling of the vorticity boundary condition (the $\psi-\omega$ formulation) and the calculation of high-order derivatives including the cross-ones (the ψ formulation). Furthermore, the pressure field needs be resolved, which is generally recognised as a complicated process. For the $\widehat{u}-p$ formulation, the pressure and velocity fields are obtained directly from the discretised equations and it is straightforward to extend the formulation to 3D problems.

It was reported (e.g. [Roache (1998); Cheng (1968); Cyrus and Fulton (1967)]) that the use of a conservative form of the governing equation has the ability to give more accurate results than the use of a non-conservative form. In [Torrance, Davis, Eike, Gill, Gutman, Hsui, Lyons, and Zien (1972)], through the simulation of a flow in a cavity, it was shown that results by using the conservative equations with first-order accurate interpolants are better than those by using the non-conservative equations with second-order accurate interpolants.

To facilitate a numerical calculation, the spatial domain needs be discretised. Generating a Cartesian grid, which is associated with finite-difference methods (FDMs), can be seen to be much more straightforward than generating a finite-element (FE) mesh, which is associated with FE and finite-volume (FV) methods.

Radial basis function networks (RBFNs) have emerged as a powerful approximation tool. They have been applied for the solution of ordinary (ODEs) and partial (PDEs) differential equations. The RBF approximations representing the field variable can be constructed through differentiation (DRBFNs) [Kansa (1990), Kansa, Power, Fasshauer, and Ling (2004)] and integration (IRBFNs) [Mai-Duy and Tran-Cong (2001)]. The latter has extra power in the implementation of multiple boundary values.

A fractional-step/projection approach, which is originally suggested by [Chorin (1968)], is widely applied for the simulation of incompressible viscous flows modelled with the $\widehat{u}-p$ formulation. Variations of this approach have been published in, for example, [Kim and Moin (1985), Van Kan (1986), Bell, Colella, and Glaz (1989), Perot (1993) and Almgren (1996)]. In this study, we will propose a numerical projection method, based on Cartesian grids and a compact local IRBF scheme, for the discretisation of the $\widehat{u}-p$ formulation in two dimensions. Boundary conditions for the pressure are taken in the form of Dirichlet type, and to do so, we propose a treatment based on global 1D IRBF approximations using values of the pressure at interior nodes along a grid line and first-order derivative values of the pressure at the two extreme nodes of that grid line. The performance of the present method is investigated numerically through the solution of linear and non-linear problems.

The remainder of the paper is organised as follows. Sections 2 and 3 briefly outline the mathematical model of incompressible viscous flows and the global 1D-IRBF approximation scheme, respectively. The proposed compact local IRBF scheme and the proposed boundary treatment for the pressure are described in Section 4. In Section 5, numerical results are presented and compared with some benchmark solutions, where appropriate. Finally, some concluding remarks are given in Section 6.

2 Mathematical model

The transient Navier-Stokes equations for an incompressible Newtonian fluid in the primitive variables can be written in the non-dimensional conservative form as

$$\nabla.\widehat{u} = 0 \tag{1}$$

$$\frac{\partial \widehat{u}}{\partial t} + \nabla.(\widehat{u}\,\widehat{u}) = -\nabla p + \frac{1}{Re}\nabla^2\widehat{u} + \widehat{b} \tag{2}$$

where $\widehat{u} = (u,v)^T$, p and $\widehat{b} = (b_x, b_y)^T$ are the velocity vector, the static pressure, and the body-force vector, respectively, defined in the Cartesian x and y system; and $Re = UL/\nu$ the Reynolds number, in which ν is the kinematic viscosity, L the characteristic length and U the characteristic speed of the flow.

For the projection method [Chorin (1968)], the velocity and the pressure variables in the above set of PDEs are solved separately in each iteration. The temporal discretisation of (2) with an explicit Euler scheme gives

$$\frac{\widehat{u}^n - \widehat{u}^{n-1}}{\Delta t} = -\nabla p^n + \frac{1}{Re}\nabla^2\widehat{u}^{n-1} - \nabla.(\widehat{u}^{n-1}\widehat{u}^{n-1}) + \widehat{b}^{n-1} \tag{3}$$

where the superscript n is used to denote the time level.

An intermediate velocity vector, denoted by $\widehat{u}^{*,n}$, is defined as

$$\frac{\widehat{u}^{*,n} - \widehat{u}^{n-1}}{\Delta t} = \frac{1}{Re}\nabla^2\widehat{u}^{n-1} - \nabla.(\widehat{u}^{n-1}\widehat{u}^{n-1}) + \widehat{b}^{n-1} \tag{4}$$

This equation, which does not involve the pressure gradient term, can be rewritten as

$$\widehat{u}^{*,n} = \widehat{u}^{n-1} + \Delta t\left[\frac{1}{Re}\nabla^2\widehat{u}^{n-1} - \nabla.(\widehat{u}^{n-1}\widehat{u}^{n-1}) + \widehat{b}^{n-1}\right] \tag{5}$$

It is seen that $\widehat{u}^{*,n}$ does not satisfy the continuity equation (1). From (3) and (4), one can derive the following equation

$$\frac{\widehat{u}^n - \widehat{u}^{*,n}}{\Delta t} = -\nabla p^n \tag{6}$$

The Poisson equation for the pressure is then obtained by applying the gradient operator to both sides of (6) and forcing $\widehat{u}^n$ to satisfy (1)

$$\nabla^2 p^n = \frac{1}{\Delta t}\nabla\cdot\widehat{u}^{*,n} \tag{7}$$

After solving (7), the velocity field at the next time level is calculated through (6) as

$$\widehat{u}^n = \widehat{u}^{*,n} - \Delta t\nabla p^n \tag{8}$$

3 A brief review of the global 1D-IRBF scheme

Consider the approximation of a univariate function $f(\eta)$ and its derivatives up to second order. The second-order derivative of f is decomposed into RBFs

$$\frac{d^2 f(\eta)}{d\eta^2} = \sum_{i=1}^{m} w_i G_i(\eta) \tag{9}$$

where m is the number of RBFs; $\{G_i(\eta)\}_{i=1}^{m}$ the set of RBFs; and $\{w_i\}_{i=1}^{m}$ the set of weights/coefficients to be found. Approximate representations for the first-order derivative and the function itself are then obtained through integration

$$\frac{df(\eta)}{d\eta} = \sum_{i=1}^{m} w_i H_i(\eta) + c_1 \tag{10}$$

$$f(\eta) = \sum_{i=1}^{m} w_i \overline{H}_i(\eta) + c_1\eta + c_2 \tag{11}$$

where $H_i(\eta) = \int G_i(\eta)d\eta$; $\overline{H}_i(\eta) = \int H_i(\eta)d\eta$; and c_1 and c_2 are the constants of integration.

Let $\{\eta_i\}_{i=1}^{q}$ $(q = m-2)$ and $\{\eta_{b1}, \eta_{b2}\}$ be a set of interior nodal points and a set of boundary nodal points, respectively, as shown in Figure 1. We choose the set of RBF centres as the set of nodes. Evaluation of (11) at the interior and boundary nodes results in

$$\begin{pmatrix} \widehat{f} \\ \widehat{f}_b \end{pmatrix} = \overline{\mathscr{H}} \begin{pmatrix} \widehat{w} \\ c_1 \\ c_2 \end{pmatrix} \tag{12}$$

where

$$\begin{aligned}
\widehat{f} &= (f_1, f_2, \cdots, f_q)^T \\
\widehat{f}_b &= (f_{b1}, f_{b2})^T \\
\widehat{w} &= (w_1, w_2, \cdots, w_m)^T \\
\overline{\mathscr{H}} &= \begin{bmatrix}
\overline{H}_1(\eta_1) & \cdots & \overline{H}_m(\eta_1) & \eta_1 & 1 \\
\overline{H}_1(\eta_2) & \cdots & \overline{H}_m(\eta_2) & \eta_2 & 1 \\
\vdots & \ddots & \vdots & \vdots & \vdots \\
\overline{H}_1(\eta_q) & \cdots & \overline{H}_m(\eta_q) & \eta_q & 1 \\
\overline{H}_1(\eta_{b1}) & \cdots & \overline{H}_m(\eta_{b1}) & \eta_{b1} & 1 \\
\overline{H}_1(\eta_{b2}) & \cdots & \overline{H}_m(\eta_{b2}) & \eta_{b2} & 1
\end{bmatrix}
\end{aligned} \tag{13}$$

The system (12), which represents the relation between the RBF space and the physical space and hereafter is called a conversion system, can be solved for the unknown vector of weights $(\widehat{w}, c_1, c_2)^T$ by means of the singular value decomposition (SVD) technique

$$\begin{pmatrix} \widehat{w} \\ c_1 \\ c_2 \end{pmatrix} = \overline{\mathscr{H}}^{-1} \begin{pmatrix} \widehat{f} \\ \widehat{f}_b \end{pmatrix} \tag{14}$$

where $\overline{\mathscr{H}}^{-1}$ is the pseudo-inverse of $\overline{\mathscr{H}}$.

Making use of (14), (10) and (9), values of the first and second derivatives of f at the interior and boundary nodes are, respectively, computed as

$$\begin{pmatrix} \frac{df_1}{d\eta} \\ \frac{df_2}{d\eta} \\ \vdots \\ \frac{df_q}{d\eta} \\ \frac{df_{b1}}{d\eta} \\ \frac{df_{b2}}{d\eta} \end{pmatrix} = \begin{bmatrix} H_1(\eta_1) & \cdots & H_m(\eta_1) & 1 & 0 \\ H_1(\eta_2) & \cdots & H_m(\eta_2) & 1 & 0 \\ \vdots & \ddots & \vdots & \vdots & \vdots \\ H_1(\eta_q) & \cdots & H_m(\eta_q) & 1 & 0 \\ H_1(\eta_{b1}) & \cdots & H_m(\eta_{b1}) & 1 & 0 \\ H_1(\eta_{b2}) & \cdots & H_m(\eta_{b2}) & 1 & 0 \end{bmatrix} \overline{\mathscr{H}}^{-1} \begin{pmatrix} \widehat{f} \\ \widehat{f}_b \end{pmatrix} \tag{15}$$

$$\begin{pmatrix} \frac{d^2f_1}{d\eta^2} \\ \frac{d^2f_2}{d\eta^2} \\ \vdots \\ \frac{d^2f_q}{d\eta^2} \\ \frac{d^2f_{b1}}{d\eta^2} \\ \frac{d^2f_{b2}}{d\eta^2} \end{pmatrix} = \begin{bmatrix} G_1(\eta_1) & \cdots & G_m(\eta_1) & 0 & 0 \\ G_1(\eta_2) & \cdots & G_m(\eta_2) & 0 & 0 \\ \vdots & \ddots & \vdots & \vdots & \vdots \\ G_1(\eta_q) & \cdots & G_m(\eta_q) & 0 & 0 \\ G_1(\eta_{b1}) & \cdots & G_m(\eta_{b1}) & 0 & 0 \\ G_1(\eta_{b2}) & \cdots & G_m(\eta_{b2}) & 0 & 0 \end{bmatrix} \overline{\mathscr{H}}^{-1} \begin{pmatrix} \widehat{f} \\ \widehat{f}_b \end{pmatrix} \tag{16}$$

These expressions can be rewritten in the following compact form

$$\widehat{\frac{df}{d\eta}} = \widehat{\mathscr{D}}_{1\eta}\,\widehat{f} + \widehat{k}_{1\eta}, \tag{17}$$

and

$$\widehat{\frac{d^2f}{d\eta^2}} = \widehat{\mathscr{D}}_{2\eta}\,\widehat{f} + \widehat{k}_{2\eta}, \tag{18}$$

where the matrices $\widehat{\mathscr{D}}_{1\eta}$ and $\widehat{\mathscr{D}}_{2\eta}$ consist of all but the last two columns of the product of two matrices on the right-hand side of (15) and (16), respectively; and

$\widehat{k}_{1\eta}$ and $\widehat{k}_{2\eta}$ are obtained by multiplying the vector $\widehat{f}_b$ with the last two columns of (15) and (16) respectively. It is noted that entries of $\widehat{k}_{1\eta}$ and $\widehat{k}_{2\eta}$ are functions of the two boundary values.

It can be seen that derivatives of the function f at nodes are expressed in terms of nodal values of f.

4 Proposed method

Consider an interior grid point (x_0, y_0) and its associated local 3-point stencil $[\eta_1, \eta_2, \eta_3]$ $(\eta_1 < \eta_2 < \eta_3,\ \eta_0 \equiv \eta_2)$ as shown in Figure 2, in which η represents x and y.

4.1 A high-order compact local IRBF scheme

Over a local 3-point stencil, we can represent the conversion system as a matrix-vector multiplication

$$\begin{pmatrix} f_1 \\ f_2 \\ f_3 \\ \frac{d^2 f_1}{d\eta^2} \\ \frac{d^2 f_3}{d\eta^2} \end{pmatrix} = \underbrace{\begin{pmatrix} \overline{\mathscr{H}} \\ \mathscr{G} \end{pmatrix}}_{\mathscr{C}} \begin{pmatrix} w_1 \\ w_2 \\ w_3 \\ c_1 \\ c_2 \end{pmatrix} \tag{19}$$

where $f_i = f(\eta_i)$ $(i = \{1,2,3\})$; $\frac{d^2 f_i}{d\eta^2} = \frac{d^2 f}{d\eta^2}(\eta_i)$ $(i = \{1,3\})$; $\mathscr{C}$ is the conversion matrix and $\overline{\mathscr{H}}$, $\mathscr{G}$ are submatrices defined as

$$\overline{\mathscr{H}} = \begin{bmatrix} \overline{H}_1(\eta_1) & \overline{H}_2(\eta_1) & \overline{H}_3(\eta_1) & \eta_1 & 1 \\ \overline{H}_1(\eta_2) & \overline{H}_2(\eta_2) & \overline{H}_3(\eta_2) & \eta_2 & 1 \\ \overline{H}_1(\eta_3) & \overline{H}_2(\eta_3) & \overline{H}_3(\eta_3) & \eta_3 & 1 \end{bmatrix} \tag{20}$$

$$\mathscr{G} = \begin{bmatrix} G_1(\eta_1) & G_2(\eta_1) & G_3(\eta_1) & 0 & 0 \\ G_1(\eta_3) & G_2(\eta_3) & G_3(\eta_3) & 0 & 0 \end{bmatrix} \tag{21}$$

Solving (19) yields

$$\begin{pmatrix} w_1 \\ w_2 \\ w_3 \\ c_1 \\ c_2 \end{pmatrix} = \mathscr{C}^{-1} \begin{pmatrix} f_1 \\ f_2 \\ f_3 \\ \frac{d^2 f_1}{d\eta^2} \\ \frac{d^2 f_3}{d\eta^2} \end{pmatrix} \tag{22}$$

which maps the vector of nodal values of the function and of its second derivative to the vector of RBF coefficients including two integration constants. Approximate

expressions for f and its derivatives in the physical space are obtained by substituting (22) into (11), (10) and (9), respectively.

$$f(\eta) = \left[\begin{array}{ccccccc} \overline{H}_1(\eta) & \overline{H}_2(\eta) & \overline{H}_3(\eta) & \eta & 1 \end{array} \right] \mathscr{C}^{-1} \left(\begin{array}{c} \widehat{f} \\ \widehat{\frac{d^2 f}{d\eta^2}} \end{array} \right) \tag{23}$$

$$\frac{df(\eta)}{d\eta} = \left[\begin{array}{ccccccc} H_1(\eta) & H_2(\eta) & H_3(\eta) & 1 & 0 \end{array} \right] \mathscr{C}^{-1} \left(\begin{array}{c} \widehat{f} \\ \widehat{\frac{d^2 f}{d\eta^2}} \end{array} \right) \tag{24}$$

$$\frac{d^2 f(\eta)}{d\eta^2} = \left[\begin{array}{ccccccc} G_1(\eta) & G_2(\eta) & G_3(\eta) & 0 & 0 \end{array} \right] \mathscr{C}^{-1} \left(\begin{array}{c} \widehat{f} \\ \widehat{\frac{d^2 f}{d\eta^2}} \end{array} \right) \tag{25}$$

where $\eta_1 \leq \eta \leq \eta_3$; $\widehat{f} = (f_1, f_2, f_3)^T$ and $\widehat{\frac{d^2 f}{d\eta^2}} = (\frac{d^2 f_1}{d\eta^2}, \frac{d^2 f_3}{d\eta^2})^T$. They can be rewritten in the form

$$f(\eta) = \sum_{i=1}^{3} \varphi_i(\eta) f_i + \varphi_4(\eta) \frac{d^2 f_1}{d\eta^2} + \varphi_5(\eta) \frac{d^2 f_3}{d\eta^2} \tag{26}$$

$$\frac{df(\eta)}{d\eta} = \sum_{i=1}^{3} \frac{d\varphi_i(\eta)}{d\eta} f_i + \frac{d\varphi_4(\eta)}{d\eta} \frac{d^2 f_1}{d\eta^2} + \frac{d\varphi_5(\eta)}{d\eta} \frac{d^2 f_3}{d\eta^2} \tag{27}$$

$$\frac{d^2 f(\eta)}{d\eta^2} = \sum_{i=1}^{3} \frac{d^2\varphi_i(\eta)}{d\eta^2} f_i + \frac{d^2\varphi_4(\eta)}{d\eta^2} \frac{d^2 f_1}{d\eta^2} + \frac{d^2\varphi_5(\eta)}{d\eta^2} \frac{d^2 f_3}{d\eta^2} \tag{28}$$

where $\{\varphi_i(\eta)\}_{i=1}^5$ is the set of IRBFs in the physical space. It can be seen from (26)-(28) that the present IRBF approximations are expressed in terms of not only nodal function values but also nodal second-derivative values.

The present compact local 3-point IRBF scheme is utilised to represent the variations of the velocity components, the intermediate velocity components and the pressure in (3)-(8).

4.2 Two boundary treatments for the pressure

In order to solve the pressure Poisson equation (7), a boundary condition for the pressure is required. On the non-slip boundaries, from the momentum equation (2), one can derive the Neumann boundary condition for the pressure as

$$\frac{\partial p_b^n}{\partial x} = \frac{1}{Re} \left(\frac{\partial^2 u_b^{n-1}}{\partial x^2} + \frac{\partial^2 u_b^{n-1}}{\partial y^2} \right) - \left(\frac{\partial (u_b^{n-1} u_b^{n-1})}{\partial x} + \frac{\partial (v_b^{n-1} u_b^{n-1})}{\partial y} \right) + b_x^{n-1} = \frac{u_b^{*,n} - u_b^n}{\Delta t} \tag{29}$$

$$\frac{\partial p_b^n}{\partial y} = \frac{1}{Re}\left(\frac{\partial^2 v_b^{n-1}}{\partial x^2} + \frac{\partial^2 v_b^{n-1}}{\partial y^2}\right) - \left(\frac{\partial (u_b^{n-1} v_b^{n-1})}{\partial x} + \frac{\partial (v_b^{n-1} v_b^{n-1})}{\partial y}\right) + b_y^{n-1} = \frac{v_b^{*,n} - v_b^n}{\Delta t} \tag{30}$$

In what follows, we will describe an implementation of the Neumann boundary condition in the context of IRBFs (Treatment 1), and present a new treatment, which transforms the Neumann boundary condition into the Dirichlet one, and its detailed implementation (Treatment 2).

4.2.1 Treatment 1

The boundary condition for the pressure is imposed in the Neumann form. Assume that η_1 is a boundary node (i.e. $\eta_{b1} \equiv \eta_1$). At the current time level n, one can calculate the value of $\partial p/\partial \eta$ at η_{b1} through (29) and (30). We modify the conversion system (19) as

$$\begin{pmatrix} p_1^n \\ p_2^n \\ p_3^n \\ \frac{\partial p_{b1}^n}{\partial \eta} \\ \frac{\partial^2 p_3^{n-1}}{\partial \eta^2} \end{pmatrix} = \begin{pmatrix} \overline{\mathscr{H}} \\ \mathscr{H} \\ \mathscr{G} \end{pmatrix} \begin{pmatrix} w_1^n \\ w_2^n \\ w_3^n \\ c_1^n \\ c_2^n \end{pmatrix} \tag{31}$$

where the superscript n is used to denote the time level; $\partial p_{b1}^n/\partial \eta$ and $\partial^2 p_3^{n-1}/\partial \eta^2$ are known values; $\overline{\mathscr{H}}$ is defined as in (20); and

$$\mathscr{H} = \begin{bmatrix} H_1(\eta_{b1}) & H_2(\eta_{b1}) & H_3(\eta_{b1}) & 1 & 0 \end{bmatrix} \tag{32}$$

$$\mathscr{G} = \begin{bmatrix} G_1(\eta_3) & G_2(\eta_3) & G_3(\eta_3) & 0 & 0 \end{bmatrix} \tag{33}$$

Equation (31) leads to

$$\begin{pmatrix} w_1^n \\ w_2^n \\ w_3^n \\ c_1^n \\ c_2^n \end{pmatrix} = \begin{pmatrix} \overline{\mathscr{H}} \\ \mathscr{H} \\ \mathscr{G} \end{pmatrix}^{-1} \begin{pmatrix} p_1^n \\ p_2^n \\ p_3^n \\ \frac{\partial p_{b1}^n}{\partial \eta} \\ \frac{\partial^2 p_3^{n-1}}{\partial \eta^2} \end{pmatrix} \tag{34}$$

It can be seen that there are two unknowns over the stencil associated with $\eta_0 \equiv \eta_2$, namely p_{b1}^n and p_2^n. As a result, apart from collocating (7) at η_2 for the unknown

p_2^n, one also needs to collocate (7) at η_{b1} for the unknown p_{b1}^n. Values of the second derivative of p at η_{b1} and η_2 at the current time level are thus computed as

$$\begin{pmatrix} \frac{\partial^2 p_{b1}^n}{\partial \eta^2} \\ \frac{\partial^2 p_2^n}{\partial \eta^2} \end{pmatrix} = \begin{bmatrix} G_1(\eta_{b1}) & \cdots & G_m(\eta_{b1}) & \eta_{b1} & 1 \\ G_1(\eta_2) & \cdots & G_m(\eta_2) & \eta_2 & 1 \end{bmatrix} \begin{pmatrix} \overline{\mathscr{H}} \\ \mathscr{H} \\ \mathscr{G} \end{pmatrix}^{-1} \begin{pmatrix} p_1^n \\ p_2^n \\ p_3^n \\ \frac{\partial p_{b1}^n}{\partial \eta} \\ \frac{\partial^2 p_3^{n-1}}{\partial \eta^2} \end{pmatrix} \tag{35}$$

4.2.2 Treatment 2

The boundary condition for the pressure is imposed in the Dirichlet form. The process of deriving Dirichlet boundary conditions for the pressure is based on the global 1D-IRBF approximation scheme, i.e. (9)-(11), using the previous values of the pressure at interior nodes along a grid line and the current first-order derivative values of the pressure at the two extreme nodes of that grid line [Thai-Quang, Le-Cao, Mai-Duy, and Tran-Cong (2011)].

Consider a grid line η and let m be the number of nodes on the grid line. From (29)-(30), one can obtain derivative values of the pressure at the two extreme nodes, i.e. $\partial p_{b1}^n/\partial \eta$ and $\partial p_{b2}^n/\partial \eta$. We modify the conversion system (12) as

$$\begin{pmatrix} \widehat{p}^{n-1} \\ \frac{\partial p_{b1}^n}{\partial \eta} \\ \frac{\partial p_{b2}^n}{\partial \eta} \end{pmatrix} = \begin{pmatrix} \overline{\mathscr{H}} \\ \mathscr{H} \end{pmatrix} \begin{pmatrix} \widehat{w}^n \\ c_1^n \\ c_2^n \end{pmatrix} \tag{36}$$

where the left-hand side is a known vector

$$\widehat{p}^{n-1} = \left(p_1^{n-1}, p_2^{n-1}, \cdots, p_q^{n-1}\right)^T \quad (q = m-2)$$
$$\widehat{w}^n = \left(w_1^n, w_2^n, \cdots, w_m^n\right)^T$$

$$\overline{\mathscr{H}} = \begin{bmatrix} \overline{H}_1(\eta_1) & \cdots & \overline{H}_m(\eta_1) & \eta_1 & 1 \\ \overline{H}_1(\eta_2) & \cdots & \overline{H}_m(\eta_2) & \eta_2 & 1 \\ \vdots & \ddots & \vdots & \vdots & \vdots \\ \overline{H}_1(\eta_q) & \cdots & \overline{H}_m(\eta_q) & \eta_q & 1 \end{bmatrix} \tag{37}$$

$$\mathscr{H} = \begin{bmatrix} H_1(\eta_{b1}) & \cdots & H_m(\eta_{b1}) & 1 & 0 \\ H_1(\eta_{b2}) & \cdots & H_m(\eta_{b2}) & 1 & 0 \end{bmatrix} \tag{38}$$

Values of the pressure at the two extreme nodes at the current time level are then estimated by collocating (11) at η_{b1} and η_{b2} and making use of (36)

$$\begin{pmatrix} p_{b1}^n \\ p_{b2}^n \end{pmatrix} = \begin{bmatrix} \overline{H}_1(\eta_{b1}) & \cdots & \overline{H}_m(\eta_{b1}) & \eta_{b1} & 1 \\ \overline{H}_1(\eta_{b2}) & \cdots & \overline{H}_m(\eta_{b2}) & \eta_{b2} & 1 \end{bmatrix} \begin{pmatrix} \overline{\mathscr{H}} \\ \mathscr{H} \end{pmatrix}^{-1} \begin{pmatrix} \widehat{p}^{n-1} \\ \frac{\partial p_{b1}^n}{\partial \eta} \\ \frac{\partial p_{b2}^n}{\partial \eta} \end{pmatrix} \tag{39}$$

We use these known values as Dirichlet boundary conditions in solving the pressure Poisson equation (7).

4.3 Solution procedure

The proposed solution procedure is outlined as follows

- Step 1: Guess initial values for the pressure and velocity fields. For the $Re = 0$ case, we use the rest state as the initial guess. For a $Re > 0$ case, we use the solution corresponding to a smaller Re as the initial guess.

- Step 2: Compute the intermediate velocity field

$$\widehat{u}^{*,n} = \widehat{u}^{n-1} + \Delta t[\frac{1}{Re}\nabla^2\widehat{u}^{n-1} - \nabla.(\widehat{u}^{n-1}\widehat{u}^{n-1}) + \widehat{f}^{n-1}] \tag{40}$$

  using the proposed compact local IRBF scheme, i.e (27)-(28), in which, for $n > 2$, nodal values of the field variable and its second derivatives are taken from the time level $(n-1)$ and $(n-2)$, respectively. It is noted that, on the boundary, some nodal second-derivative values are estimated through the governing equations, e.g.
  $\frac{\partial^2 u_b^{n+1}}{\partial x^2}$, $\frac{\partial^2 v_b^{n+1}}{\partial x^2}$, $\frac{\partial^2 u_b^{n+1}}{\partial y^2}$ and $\frac{\partial^2 v_b^{n+1}}{\partial y^2}$
  and some through the global 1D-IRBF scheme, e.g.
  $\frac{\partial^2 (uu)_b^{n+1}}{\partial x^2}$, $\frac{\partial^2 (uv)_b^{n+1}}{\partial x^2}$, $\frac{\partial^2 u_b^{*(n+1)}}{\partial x^2}$, $\frac{\partial^2 p_b^{n+1}}{\partial x^2}$, $\frac{\partial^2 (vu)_b^{n+1}}{\partial y^2}$, $\frac{\partial^2 (vv)_b^{n+1}}{\partial y^2}$, $\frac{\partial^2 v_b^{*(n+1)}}{\partial y^2}$ and $\frac{\partial^2 p_b^{n+1}}{\partial y^2}$.

- Step 3: Compute $\nabla.\widehat{u}^{*,n}$ according to the formula (27), in which, for $n > 1$, nodal values of the function and its second derivatives are taken from the time level n and $(n-1)$, respectively.

- Step 4: Compute the pressure gradients on the boundary from the momentum equations

$$\nabla p^n = \frac{1}{\Delta t}(\widehat{u}^{*,n} - \widehat{u}^{n-1}) \tag{41}$$

- Step 5: Derive a Dirichlet boundary condition for the pressure, i.e. p_b^n, in the case of using Treatment 2. Otherwise, skip this step.
- Step 6: Solve the pressure Poisson equation

$$\nabla^2 p^n = \frac{1}{\Delta t}\nabla.\widehat{u}^{*,n} \tag{42}$$

  subject to the corresponding boundary conditions.
- Step 7: Compute ∇p^n using (27) and estimate the velocity field at the current time level

$$\widehat{u}^n = \widehat{u}^{*,n} - \Delta t \nabla p^n \tag{43}$$

- Step 8: Check to see whether the flow reaches a steady state. If not, repeat from Step 2. Otherwise, stop and output the results.

5 Numerical examples

It has generally been accepted that, among RBFs, the multiquadric (MQ) scheme tends to result in the most accurate approximation [Franke (1982)]. We choose MQ as the basis function in the present calculations

$$G_i(\widehat{x}) = \sqrt{(\widehat{x}-\widehat{c}_i)^T(\widehat{x}-\widehat{c}_i)+a_i^2} \tag{44}$$

where $\widehat{x} = (x,y)^T$ is the position vector of the point of interest; $\widehat{c}_i = (x_{c_i}, y_{c_i})^T$ and a_i the position vector of the centre and the width of the ith MQ, respectively. For each stencil, the set of nodal points is taken to be the set of MQ centres. We simply choose the MQ width as $a_i = \beta h_i$ in which β is a given positive number and h_i the distance between the ith node and its nearest neighbouring node. We assess the performance of the proposed method through two measures:

(i) the root mean square (RMS) error defined as

$$Ne(u) = \frac{\sqrt{\sum_{i=1}^{N}(u_i - \overline{u}_i)^2}}{\sqrt{N}} \tag{45}$$

where N is the number of nodes over the whole domain and $\overline{u}$ is the exact solution, and

(ii) the convergence rate α with respective to grid refinement defined through $Ne \approx O(h^\alpha)$ as

$$\alpha = \frac{\log(Ne^{(r)}/Ne^{(s)})}{\log(h^{(r)}/h^{(s)})} \tag{46}$$

where h is the grid size; the superscripts (r) and (s) indicate the data obtained from the rth and sth calculations ($r < s$), respectively.

The proposed method is verified through the solution of a linear second-order ODE and the simulation of viscous flows to obtain their structures at the steady state. For the latter, the steady state is considered to have been reached when

$$\frac{\sqrt{\sum_{i=1}^{N}(u_i^{n+1}-u_i^n)^2}}{\sqrt{N}} < 10^{-9} \tag{47}$$

5.1 Ordinary differential equation (ODE)

As a first test, we consider the following boundary-value second-order problem

$$\frac{d^2u}{dx^2} = -(2\pi)^2 \sin(2\pi x), \quad 0 \le x \le 1, \quad u(0) = u(1) = 0 \tag{48}$$

The exact solution to this problem can be verified to be $\bar{u}(x) = \sin(2\pi x)$. We add a pseudo time-derivative term to equation (48) to facilitate an iterative calculation

$$\frac{d^2u}{dx^2} = -(2\pi)^2 \sin(2\pi x) + \frac{du}{dt} \tag{49}$$

When the difference of u between two successive time levels is small, i.e. $\frac{du}{dt} \simeq 0$ (the iterative process is said to converge), the obtained solution is also a solution to (48).

In the present calculation, a time step of 0.5 is used. It is noted that the higher the value of a permissible time step, the faster the convergence of the solution will be. One can reduce the grid size h and/or vary the MQ width β to enhance the solution accuracy.

For $\beta-$adaptivity study, the value of β is chosen in a wide range of 2-100. Results obtained at a grid of 51 are shown in Figure 3. As β increases, the error $Ne(u)$ reduces significantly. However, at very large values of β, the behaviour of Ne becomes unstable. It appears that the optimal value of β is 8 and the corresponding condition number of the system matrix is 5.84×10^8. It is noted that, from a theoretical point of view, it is still not clear how to choose the optimal value of the MQ width. Unlike global IRBF versions (where β=1 is a preferred value), the present compact IRBF scheme can work well with a wide range of β ($20 \le \beta \le 60$).

For $h-$adaptivity study, the present IRBF and standard second-order FD calculations are conducted on various sets of uniformly distributed points, from 5 to 51 with an increment of 2. Results obtained by the two methods are given in Figure 4. It can be seen that the present scheme outperforms the FDM in terms of the solution accuracy and convergence rate, whereas the two schemes have similar values of the matrix condition number.

5.2 Analytic Stokes flow

Consider a Stokes flow [Fadel and Agouzoul (2011)]. Equations (1)-(2) reduce to

$$\nabla.\widehat{u} = 0 \tag{50}$$
$$\frac{\partial \widehat{u}}{\partial t} = -\nabla p + \nabla^2 \widehat{u} + \widehat{b} \tag{51}$$

The exact solution is chosen as

$$u(x,y) = 2\pi x^2(1-x)^2 \sin(\pi y)\cos(\pi y) \tag{52}$$
$$v(x,y) = -2x(x-1)(2x-1)\sin^2(\pi y) \tag{53}$$
$$p(x,y) = \sin(x)\cos(y) \tag{54}$$

from which, one can derive the corresponding body force

$$b_x = 2\pi(-1+6x+2(\pi^2-3)x^2-4\pi^2x^3+2\pi^2x^4)\sin(2\pi y)+\cos(x)\cos(y) \tag{55}$$
$$b_y = 4\pi^2 x(1-3x+2x^2)\cos(2\pi y)-12(1-2x)\sin^2(\pi y)-\sin(x)\sin(y) \tag{56}$$

Let $\Omega = [0,1]\times[0,1]$ be the flow domain. Values of u and v are prescribed on the boundaries according to (52) and (53), respectively, whereas the hydrostatic pressure mode is eliminated by fixing the pressure value at a single node. In the present study, we take the centre of the cavity as a reference point.

The simulations are performed for a set of grids, $\{11\times 11, 21\times 21, \cdots, 51\times 51\}$. In Table 1, we present an accuracy analysis with respect to grid refinement for results obtained by the proposed scheme and the standard second-order central FD scheme. It can be seen that the former outperforms the latter regarding both the solution accuracy and the rate of convergence. The overall convergence rates are 3.01 for u, 3.11 for v and 2.88 for p by the proposed scheme, while the corresponding values are 2.09, 2.18 and 2.78 by the FDM.

5.3 Recirculating cavity flow driven by combined shear and body forces

This problem is taken from [Shih and Tan (1989)]. The recirculating flow of a Newtonian fluid in a square cavity (Figure 5) is induced by the combined shear and body forces. The governing equations are of the form (1)-(2). It is assumed that the velocity profile along the top boundary is $v = 0$ and $u(x,1) = 16x^2(x-1)^2$ while the other walls are non-slip and stationary. The body force, which is present in the

y-direction only, is given by

$$b_x = 0 \tag{57}$$

$$b_y = -\frac{8}{Re}[24F(x) + 2f'(x)g''(y) + f'''(x)g(y)] - 64[F_2(x)G_1(y) - g(y)g'(y)F_1(x)] \tag{58}$$

where

$f(x) = x^4 - 2x^3 + x^2$

$g(y) = y^4 - y^2$

$F(x) = \int f(x)dx = 0.2x^5 - 0.5x^4 + x^3/3$

$F_1(x) = f(x)f''(x) - [f'(x)]^2 = -4x^6 + 12x^5 - 14x^4 + 8x^3 - 2x^2$

$F_2(x) = \int f(x)f'(x)dx = 0.5[f(x)]^2$

$G_1(y) = g(y)g'''(y) - g'(y)g''(y) = -24y^5 + 8y^3 - 4y$

The exact solution to this problem is known to be

$$u(x,y) = 8f(x)g'(y) = 8(x^4 - 2x^3 + x^2)(4y^3 - 2y), \tag{59}$$

$$v(x,y) = -8f'(x)g(y) = -8(4x^3 - 6x^2 + 2x)(y^4 - y^2), \tag{60}$$

$$p(x,y,Re) = \frac{8}{Re}[F(x)g'''(y) + f'(x)g'(y)] + 64F_2(x)[g(y)g''(y) - [g'(y)]^2]. \tag{61}$$

We employ several grids, $\{21 \times 21, 31 \times 31, \cdots, 71 \times 71\}$, and the two previously discussed boundary treatments for the pressure to simulate the flow. Table 2 compares the present results with those obtained by FD approximation schemes. In the case of IRBFs, the imposition of the pressure boundary condition in the Dirichlet form (Treatment 2) yields more accurate results than those in the Neumann form (Treatment 1). In the case of FDs, the two treatments have similar performances. The IRBF solutions are seen to be more accurate and to converge faster than the FD ones. To achieve a similar level of accuracy, the FDM requires a denser grid than the proposed scheme. For example, with Treatment 1, RMS errors of the p solution are 2.9×10^{-4} using a grid of 61×61 for the former and 2.8×10^{-4} using a grid of 21×21 for the latter. Figure 6 shows profiles of the velocity on the horizontal and vertical centrelines of the cavity, which are in very good agreement with the exact solution.

5.4 Lid-driven cavity flow

It differs from the previous problem in that the velocity of the lid is now prescribed as $\widehat{u} = (1,0)^T$ and the body force components are set to zeros. There are thus two values of u at the two top corners, making the stress solution there singular.

The singular lid-driven cavity flow is widely used as a test problem for the assessment of accuracy of numerical solvers in CFD. From the literature, FD results using very dense grids by [Ghia, Ghia, and Shin (1982)] and pseudo-spectral results by [Botella and Peyret (1998)] have been often cited for comparison purposes. It is noted that for the latter, the field variables were decomposed into the regular part that is approximated with Chebyshev polynomials and the singular part that is treated analytically; and a benchmark spectral solution for $Re = 100$ and $Re = 1000$ were provided.

We use Treatment 2 only in the imposition of the pressure boundary condition. A wide range of *Re*, $\{100, 400, 1000, 3200\}$ and uniform grids, $\{11 \times 11, 31 \times 31, 51 \times 51, 71 \times 71, 91 \times 91, 111 \times 111, 129 \times 129\}$ are considered in the simulation. The time step is chosen in the range of 0.1 to 0.00025. Smaller time steps are employed for higher *Re* and higher grid densities. Tables 3, 4 and 5 show the present results for the extrema of the velocity profiles along the centrelines of the cavity for several Reynolds numbers in comparison with some others [Ghia, Ghia, and Shin (1982); Deng, Piqueta, Queuteya, and Visonneaua (1994); Botella and Peyret (1998); Sahin and Owens (2003); Bruneau and Saad (2006)]. For $Re = 100$ (Table 3) and $Re = 1000$ (Table 4), the "errors" are calculated relative to a "benchmark" solution [Botella and Peyret (1998)], which shows that the present results are very comparable with others. Velocity profiles along the vertical and horizontal centrelines for different grid sizes at $Re = 1000$ are displayed in Figure 7, where a grid convergence of the IRBF solution is clearly observed (i.e. the present solution approaches the benchmark solution very fast as the grid density is increased). We virtually achieve the benchmark solution with only 91×91 grid in comparison with a grid of 129×129 used to obtain the benchmark solution in [Ghia, Ghia, and Shin (1982)]. In addition, those velocity profiles at $Re = \{100, 400, 1000, 3200\}$ with the grid of 129×129 are also shown in Figure 8, where the present solutions match the benchmark ones very well.

Figure 9 exhibits the distributions of the pressure for the flow at $Re = \{100, 400, 1000, 3200\}$ which look feasible in comparison with those reported in the literature. We also show streamlines and iso-vorticity lines, which are derived from the velocity field, for the flow at $Re = \{100, 400, 1000, 3200\}$ in Figure 10 and 11, where secondary vortices are well captured.

6 Concluding remarks

In this paper, we propose a high-order compact local IRBF scheme for the discretisation of the pressure-velocity formulation in the Cartesian-grid point-collocation framework. Two boundary treatments for the pressure, one is based on values of the pressure and the other based on normal derivative values of the pressure, are

studied. Like FDMs, the present approximations involve 3 nodes in each direction, resulting in a sparse system matrix. Numerical examples indicate that (i) the present results are superior to the FD results in terms of the solution accuracy and the convergence rate with grid refinement, and (ii) the imposition of boundary conditions for the pressure yields better results in the Dirichlet form than in the Neumann form.

Acknowledgement: The first author would like to thank USQ, FoES and CESRC for a postgraduate research scholarship. This work was supported by the Australian Research Council.

References

Abdallah, S. (1987): Numerical solutions for the incompressible navier-stokes equations in primitive variables using a non-staggered grid, II. *Journal of Computational Physics*, vol. 70, no. 1, pp. 193–202.

Almgren, A. S. (1996): A numerical method for the incompressible navier-stokes equations based on an approximate projection. *SIAM J. Sci. Compt.*, vol. 17.

Bell, J.; Colella, P.; Glaz, H. (1989): A second-order projection method for the incompressible navier-stokes equations. *Journal of Computational Physics*, vol. 85, no. 2, pp. 257–283.

Botella, O.; Peyret, R. (1998): Benchmark spectral results on the lid-driven cavity flow. *Computers & Fluids*, vol. 27, no. 4, pp. 421–433.

Bruneau, C.; Saad, M. (2006): The 2d lid-driven cavity problem revisited. *Computers and Fluids*, vol. 35, no. 3, pp. 326–348.

Cheng, S. I. (1968): *Accuracy of difference formulation of Navier-Stokes equations*. A. M. S. Department, Princeton University, Princeton, New Jersey.

Chorin, A. (1968): Numerical solution of the navier-stokes equations. *Mathematics of Computation*, vol. 22, no. 104, pp. 745–762.

Cyrus, N. J.; Fulton, R. E. (1967): *Accuracy study of finite difference methods*. NASA TN D-4372, National Aeronautics and Space Administration, Langley Research Centre, Langley Station, Hampton, Virginia.

Deng, G. B.; Piqueta, J.; Queuteya, P.; Visonneaua, M. (1994): Incompressible flow calculations with a consistent physical interpolation finite volume approach. *Computers & Fluids*, vol. 23, no. 8, pp. 1029–1047.

Fadel, H.; Agouzoul, M. (2011): High-order finite difference schemes for incompressible flows. *International Journal for Numerical Methods in Fluids*, vol. 65, no. 9, pp. 1050–1070.

Franke, R. (1982): Scattered data interpolation: Tests of some method. *Mathematics of Computation*, vol. 38, pp. 181–200.

Ghia, U.; Ghia, K. N.; Shin, C. (1982): High-re solutions for incompressible flow using the navier-stokes equations and a multigrid method. *Journal of Computational Physics*, vol. 48, no. 3, pp. 387–411.

Kansa, E. J. (1990): Multiquadrics- A scattered data approximation scheme with applications to computational fluid-dynamics-I. surface approximations and partial derivative estimates. *Computers and Mathematics with Applications*, vol. 19, no. 8/9, pp. 127–145.

Kansa, E. J.; Power, H.; Fasshauer, G. E.; Ling, L. (2004): A volumetric integral radial basis function method for time-dependent partial differential equations: I formulation. *Engineering Analysis with Boundary Elements*, vol. 28, pp. 1191–1206.

Kim, J.; Moin, P. (1985): Application of a fractional-step method to incompressible navier-stokes equations. *Journal of Computational Physics*, vol. 59, no. 2, pp. 308–323.

Mai-Duy, N.; Tran-Cong, T. (2001): Numerical solution of differential equations using multiquadric radial basic function networks. *Neural Networks*, vol. 14, pp. 185–199.

Perot, J. (1993): An analysis of the fractional step method. *Journal of Computational Physics*, vol. 108, no. 1, pp. 51–58.

Roache, P. J. (1998): *Fundamentals of Computational Fluid Dynamics*. Hermosa Publishers.

Sahin, M.; Owens, R. (2003): A novel fully implicit finite volume method applied to the lid-driven cavity problem - part i: High reynolds number flow calculations. *International Journal for Numerical Methods in Fluids*, vol. 42, no. 1, pp. 57–77.

Shih, T. M.; Tan, C. H. (1989): Effects of grid staggering on numerical schemes. *International Journal for Numerical Methods in Fluids*, vol. 9, no. 2, pp. 193–212.

Thai-Quang, N.; Le-Cao, K.; Mai-Duy, N.; Tran-Cong, T. (2011): Discretisation of the velocity-pressure formulation with integrated radial-basis-function networks. *Structural Longevity*, vol. 6, no. 2, pp. 77–92.

Torrance, K.; Davis, R.; Eike, K.; Gill, P.; Gutman, D.; Hsui, A.; Lyons, S.; Zien, H. (1972): Cavity flows driven by bouyancy and shear. *Journal of Fluid Mechanics*, vol. 51, no. part2, pp. 221–231.

Van Kan, J. (1986): A second-order accurate pressure-correction scheme for viscous incompressible flow. *SIAM Journal on Scientific and Statistical Computing*, vol. 7, pp. 870.

Table 1: Example 2, Stokes flow: RMS errors, local and overall convergence rates for u, v and p by the proposed method and FDM. The overall convergence rate α are presented in the form of $O(h^{\alpha})$.

Grid	$Ne(u)$	Rate	$Ne(v)$	Rate	$Ne(p)$	Rate
			Present method			
11×11	6.5648E-04	—-	5.3296E-04	—-	1.7813E-02	—-
21×21	8.3206E-05	2.98	6.0128E-05	3.15	2.3210E-03	2.94
31×31	2.4489E-05	3.02	1.6978E-05	3.12	7.2212E-04	2.88
41×41	1.0289E-05	3.01	7.0329E-06	3.06	3.2314E-04	2.80
51×51	5.1893E-06	3.07	3.6338E-06	2.96	1.7496E-04	2.75
		$O(h^{3.01})$		$O(h^{3.11})$		$O(h^{2.88})$
			FDM			
11×11	3.9284E-03	—-	1.3077E-03	—-	5.8633E-02	—-
21×21	8.7393E-04	2.17	2.0142E-04	2.70	7.0630E-03	3.05
31×31	3.8109E-04	2.05	9.6704E-05	1.81	2.3485E-03	2.72
41×41	2.1146E-04	2.05	5.8460E-05	1.75	1.1005E-03	2.63
51×51	1.3579E-04	1.98	3.7685E-05	1.97	6.8175E-04	2.15
		$O(h^{2.09})$		$O(h^{2.18})$		$O(h^{2.78})$

Table 2: Example 3, Recirculating cavity flow, $Re = 100$: RMS errors and local convergence rates for u, v and p

	Present (Dirichlet)		Present (Neumann)		FDM (Dirichlet)		FDM (Neumann)	
Grid	$Ne(u)$	Rate	$Ne(u)$	Rate	$Ne(u)$	Rate	$Ne(u)$	Rate
21×21	3.7323E-04	—-	6.8994E-04	—-	2.7515E-03	—-	2.8806E-03	—-
31×31	8.8758E-05	3.54	3.0028E-04	2.05	1.2587E-03	1.93	1.2598E-03	2.04
41×41	3.3153E-05	3.42	1.8214E-04	1.74	7.2116E-04	1.94	7.1861E-04	1.95
51×51	1.6052E-05	3.25	1.0607E-04	2.42	4.7417E-04	1.88	4.7156E-04	1.89
61×61	8.8940E-06	3.24	6.6161E-05	2.59	3.3465E-04	1.91	3.3254E-04	1.92
71×71	5.2855E-06	3.38	3.8683E-05	3.48	2.5021E-04	1.89	2.4875E-04	1.88
Grid	$Ne(v)$	Rate	$Ne(v)$	Rate	$Ne(v)$	Rate	$Ne(v)$	Rate
21×21	3.0814E-04	—-	1.1666E-03	—-	3.3290E-03	—-	3.0724E-03	—-
31×31	6.9064E-05	3.69	4.3065E-04	2.46	1.5300E-03	1.92	1.5246E-03	1.73
41×41	2.7564E-05	3.19	2.3730E-04	2.07	8.7191E-04	1.95	8.9158E-04	1.86
51×51	1.3899E-05	3.07	1.3227E-04	2.62	5.5126E-04	2.05	5.6429E-04	2.05
61×61	8.2254E-06	2.88	7.9870E-05	2.77	3.8059E-04	2.03	3.8919E-04	2.04
71×71	5.2222E-06	2.95	4.6700E-05	3.48	2.7666E-04	2.07	2.8119E-04	2.11
Grid	$Ne(p)$	Rate	$Ne(p)$	Rate	$Ne(p)$	Rate	$Ne(p)$	Rate
21×21	2.8508E-04	—-	7.3830E-04	—-	2.5036E-03	—-	5.8569E-03	—-
31×31	6.2890E-05	3.73	2.9702E-04	2.25	1.1474E-03	1.92	2.7822E-03	1.84
41×41	2.3775E-05	3.38	1.7771E-04	1.79	6.5178E-04	1.97	1.5035E-03	2.14
51×51	1.2035E-05	3.05	1.0679E-04	2.28	4.1769E-04	1.99	9.5988E-04	2.01
61×61	7.0999E-06	2.89	6.7371E-05	2.53	2.9038E-04	1.99	6.6316E-04	2.03
71×71	4.5087E-06	2.95	4.0092E-05	3.37	2.1349E-04	2.00	4.9218E-04	1.93

Table 3: Example 4, Lid-driven cavity flow, $Re = 100$: Extrema of the vertical and horizontal velocity profiles along the horizontal and vertical centrelines, respectively, of the cavity. "Errors" are relative to the "Benchmark" solution.

Method	Grid	u_{min}	Error (%)	y_{min}	v_{max}	Error (%)	x_{max}	v_{min}	Error (%)	x_{min}
Present	11×11	-0.1912173	10.66	0.4807	0.1595908	11.13	0.2307	-0.2236027	11.90	0.8136
Present	31×31	-0.2102259	1.78	0.4578	0.1768808	1.50	0.2370	-0.2501843	1.43	0.8107
Present	51×51	-0.2121503	0.88	0.4579	0.1781849	0.77	0.2372	-0.2520400	0.69	0.8107
FDM ($\psi - \omega$) [Ghia]	129×129	-0.2109	1.47	0.4531	0.17527	2.40	0.2344	-0.24533	3.34	0.8047
FDM ($\widehat{u} - p$) [Bruneau]	129×129	-0.2106	1.61	0.4531	0.1786	0.54	0.2344	-0.2521	0.67	0.8125
FVM ($\widehat{u} - p$) [Sahin]	257×257	-0.213924	0.06	0.4598	0.180888	0.73	0.2354	-0.256603	1.10	0.8127
FVM ($\widehat{u} - p$),cpi. [Deng]	128×128	-0.21315	0.42	—	0.17896	0.34	—	-0.25339	0.16	—
Benchmark [Botella]		-0.2140424		0.4581	0.1795728		0.2370	-0.2538030		0.8104

Table 4: Example 4, Lid-driven cavity flow, $Re = 1000$: Extrema of the vertical and horizontal velocity profiles along the horizontal and vertical centrelines, respectively, of the cavity. "Errors" are relative to the "Benchmark" solution.

Method	Grid	u_{min}	Error (%)	y_{min}	v_{max}	Error (%)	x_{max}	v_{min}	Error (%)	x_{min}
Present	51×51	-0.3629562	6.59	0.1787	0.3515585	6.73	0.1637	-0.4898251	7.07	0.9052
Present	71×71	-0.3755225	3.36	0.1753	0.3637009	3.51	0.1608	-0.5086961	3.49	0.9078
Present	91×91	-0.3815923	1.80	0.1735	0.3698053	1.89	0.1594	-0.5174658	1.82	0.9085
Present	111×111	-0.3840354	1.17	0.1728	0.3722634	1.24	0.1588	-0.5209683	1.16	0.9088
Present	129×129	-0.3848064	0.97	0.1724	0.3729119	1.07	0.1586	-0.5223350	0.90	0.9089
FDM ($\psi - \omega$) [Ghia]	129×129	-0.38289	1.46	0.1719	0.37095	1.59	0.1563	-0.5155	2.20	0.9063
FDM ($\widehat{u} - p$) [Bruneau]	256×256	-0.3764	3.13	0.1602	0.3665	2.77	0.1523	-0.5208	1.19	0.9102
FVM($\widehat{u} - p$),cpi. [Deng]	128×128	-0.38511	0.89	—	0.37369	0.86	—	-0.5228	0.81	—
Benchmark [Botella]		-0.3885698		0.1717	0.3769447		0.1578	-0.5270771		0.0908

Table 5: Example 4, Lid-driven cavity flow: Extrema of the vertical and horizontal velocity profiles along the horizontal and vertical centrelines, respectively, of the cavity at different Reynolds numbers $Re = \{400, 3200\}$.

Re	Method	Grid	u_{min}	y_{min}	v_{max}	x_{max}	v_{min}	x_{min}
400	Present	31×31	-0.316205	0.2833	0.293696	0.2236	-0.435578	0.8583
	Present	51×51	-0.323158	0.2814	0.297493	0.2248	-0.442770	0.8605
	Present	71×71	-0.325168	0.2804	0.300818	0.2252	-0.449146	0.8620
	FDM ($\psi - \omega$) [Ghia]	129×129	-0.32726	0.2813	0.30203	0.2266	-0.44993	0.8594
	FVM($\widehat{u} - p$),cpi. [Deng]	128×128	-0.32751	—	0.30271	—	-0.45274	—
	FVM($\widehat{u} - p$) [Sahin]	257×257	-0.328375	0.2816	0.304447	0.2253	-0.456316	0.8621
3200	Present	91×91	-0.406818	0.0983	0.403852	0.1016	-0.528864	0.9451
	Present	111×111	-0.418545	0.0962	0.415776	0.0995	-0.544789	0.9462
	Present	129×129	-0.423061	0.0963	0.420565	0.0994	-0.551563	0.9466
	FDM ($\psi - \omega$) [Ghia]	129×129	-0.41933	0.1016	0.42768	0.0938	-0.54053	0.9453
	FVM($\widehat{u} - p$) [Sahin]	257×257	-0.435402	0.0921	0.432448	0.0972	-0.569145	0.9491

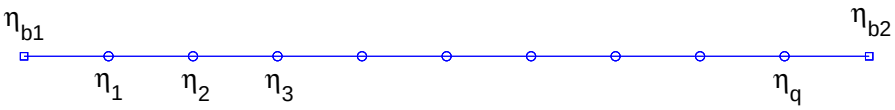

Figure 1: 1D-IRBF centres on a Cartesian grid line.

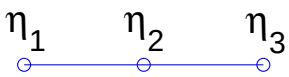

Figure 2: Local 3-point 1D-IRBF stencil.

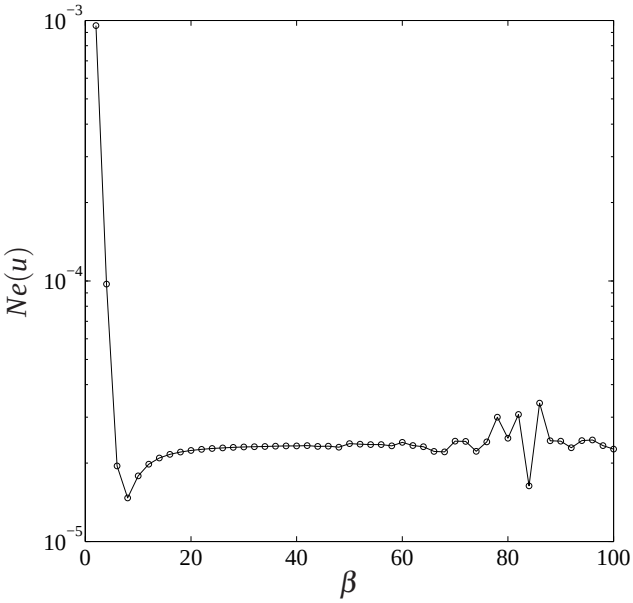

Figure 3: Example 1, ODE, $N = 51$: the effects of the MQ width β on the solution accuracy.

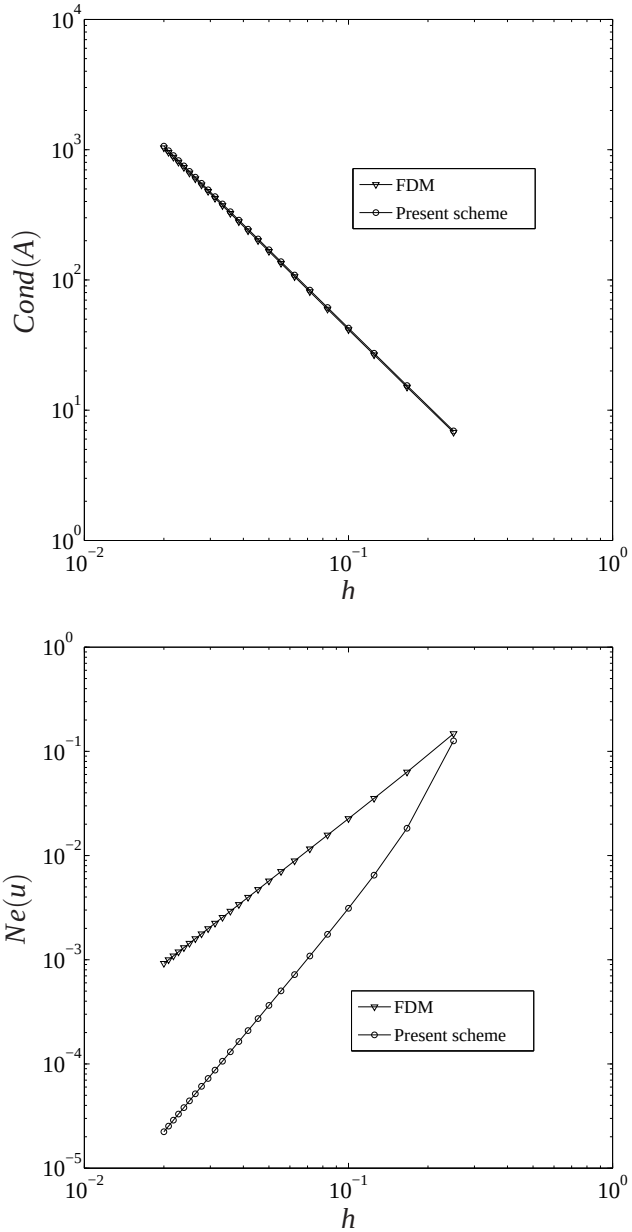

Figure 4: Example 1, ODE, $\beta = 20$, $N = \{5,7,9,...,51\}$: the effects of the grid size h on the system matrix condition (left) and the solution accuracy (right) for the FDM and the present scheme. The matrix condition number grows as $O(h^{-2})$ for the two methods while the solution converges as $O(h^2)$ for FDM and $O(h^{3.23})$ for the IRBF method.

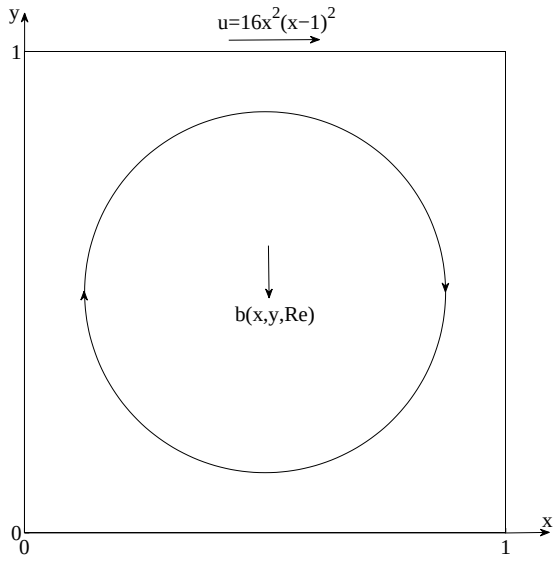

Figure 5: Example 3, Recirculating cavity flow: A schematic diagram of the physical domain (non-dimensionalised).

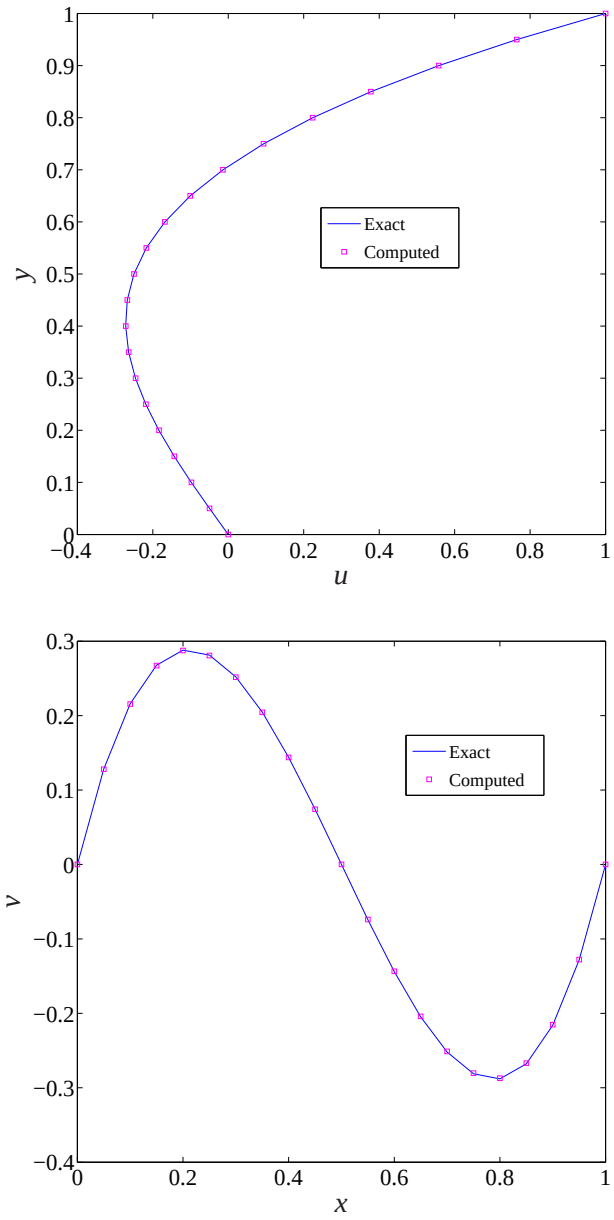

Figure 6: Example 3, Recirculating cavity flow, Treatment 2, $Re = 100$: Variations of u along the vertical centreline and of v along the horizontal centreline by the present scheme using a grid of 21×21 and the exact solution.

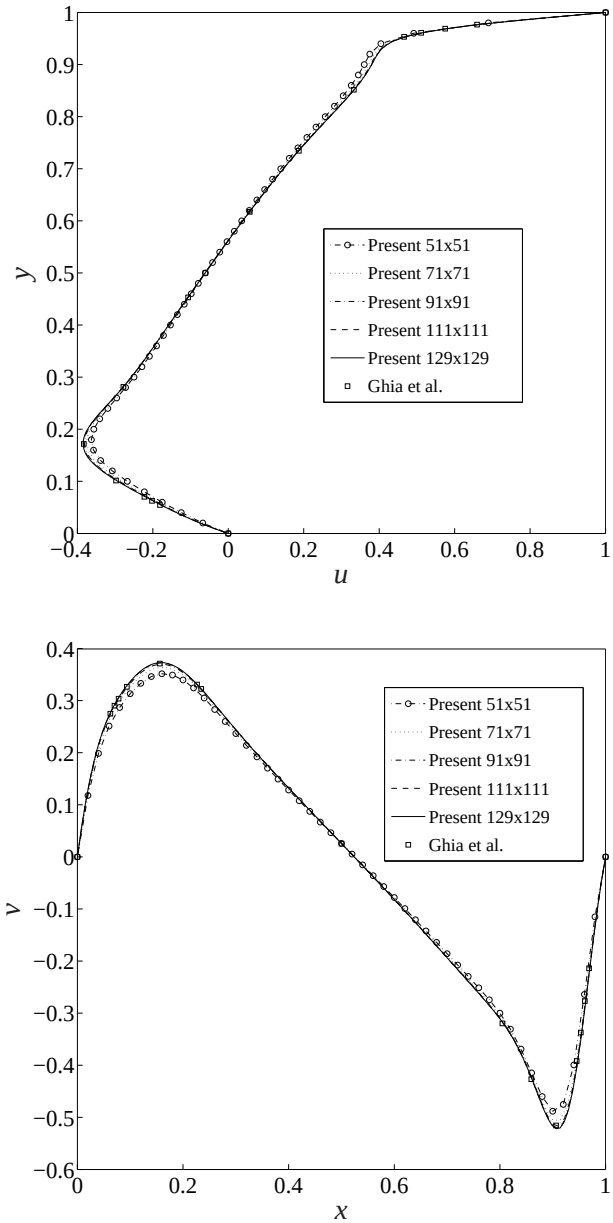

Figure 7: Example 4, Lid-driven cavity flow, $Re = 1000$: Profiles of the u-velocity along the vertical centreline and the v-velocity along the horizontal centreline using several grids. Note that curves for the last three grids are indistinguishable and agree well with the benchmark FD results.

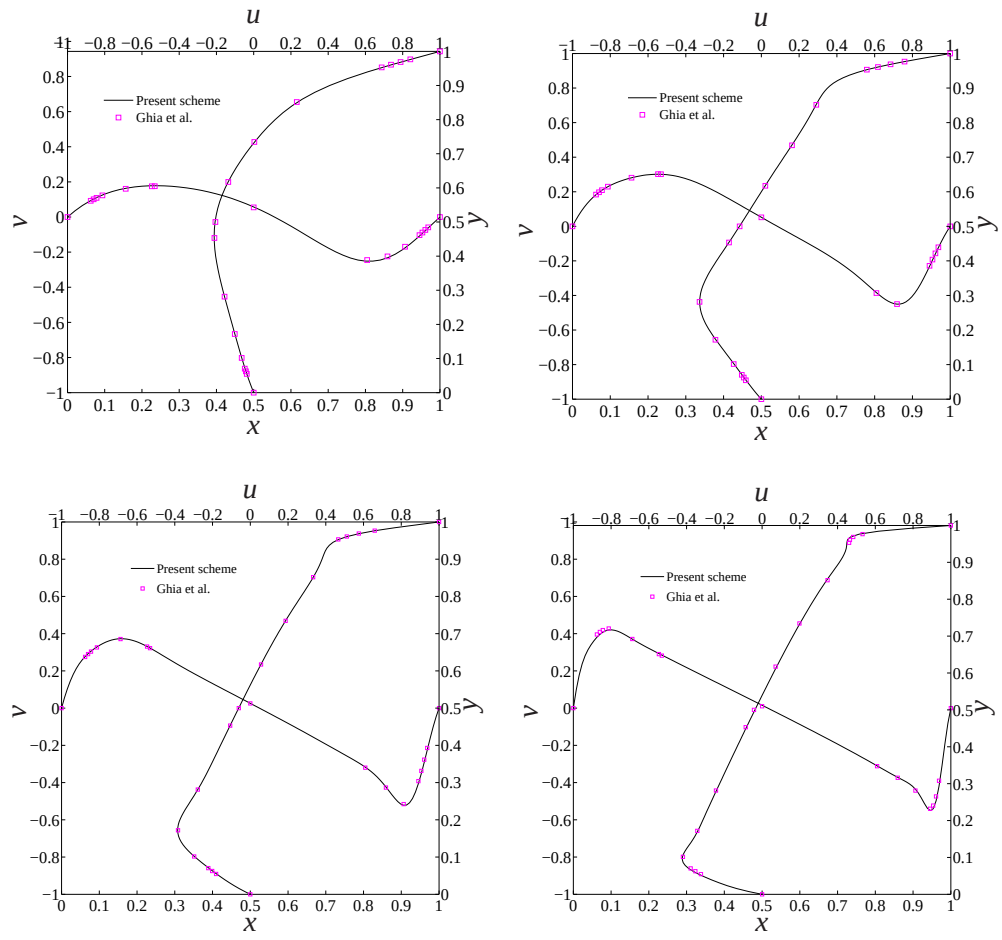

Figure 8: Example 4, Lid-driven cavity flow, 129×129: Profiles of the u-velocity along the vertical centreline and the v-velocity along the horizontal centreline for $Re = 100$ (top-left), $Re = 400$ (top-right), $Re = 1000$ (bottom-left) and $Re = 3200$ (bottom-right).

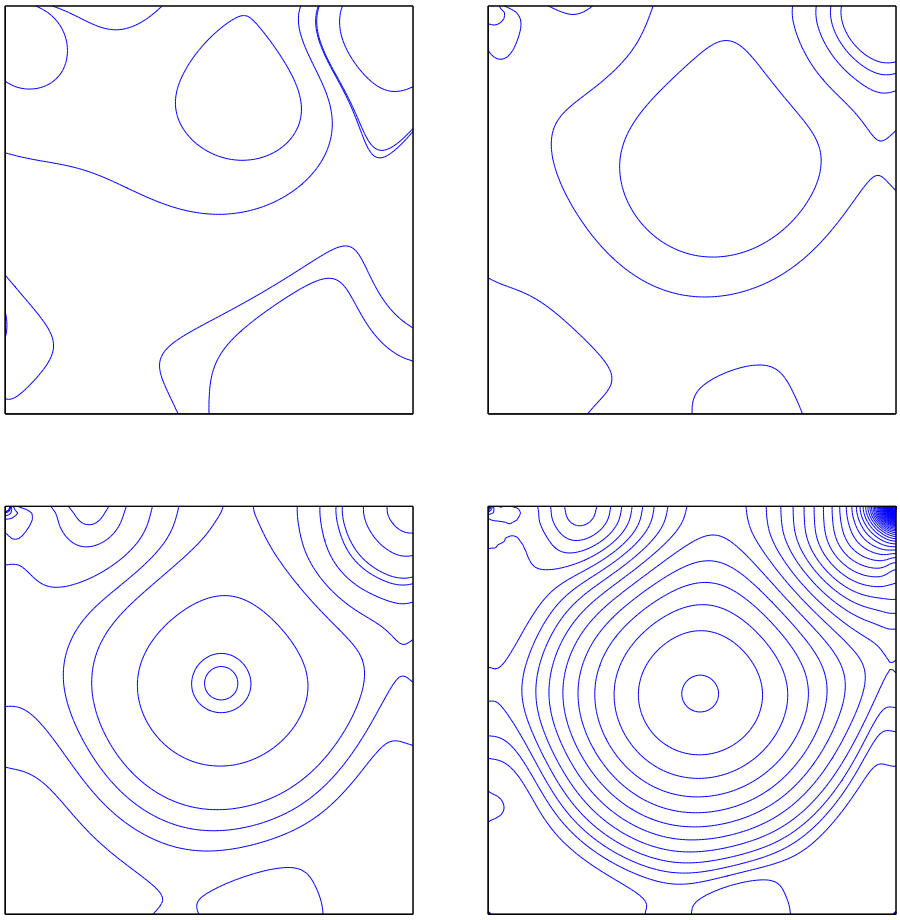

Figure 9: Example 4, Lid-driven cavity flow, 129×129: Isobaric lines of the flow for $Re = 100$ (top-left), $Re = 400$ (top-right), $Re = 1000$ (bottom-left) and $Re = 3200$ (bottom-right). The contour values used here are taken to be the same as those in [Abdallah (1987)], [Botella and Peyret (1998)] and [Bruneau and Saad (2006)]

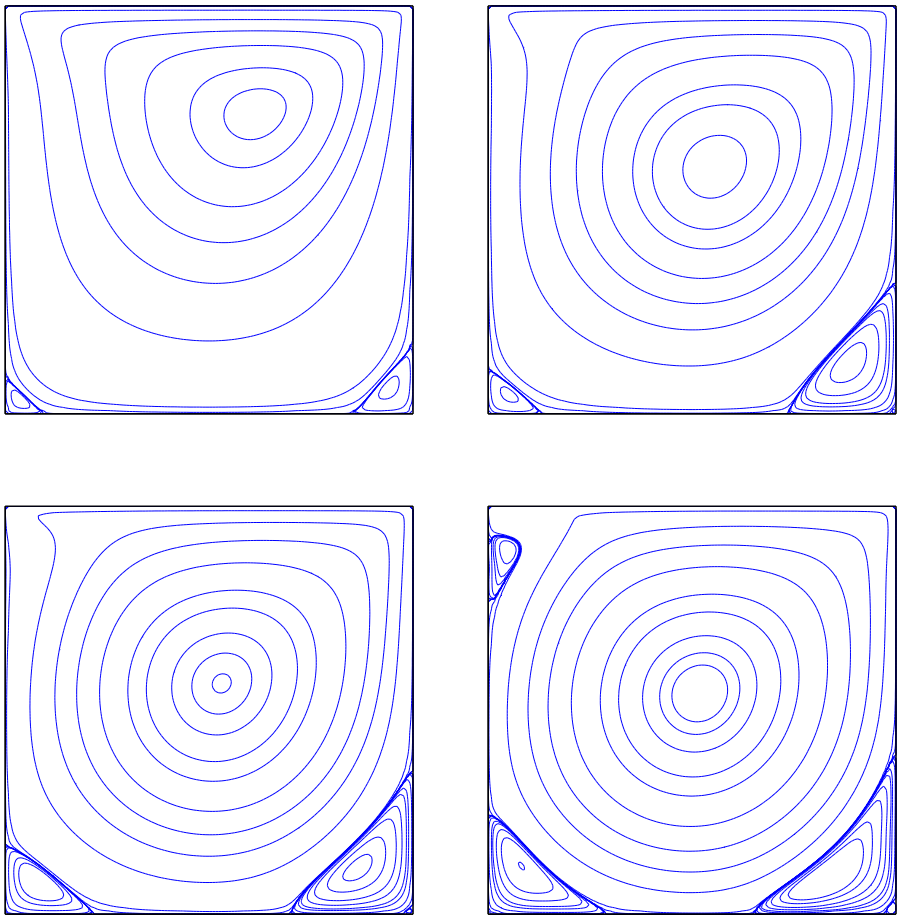

Figure 10: Example 4, Lid-driven cavity flow, 129×129: Streamlines of the flow for $Re = 100$ (top-left), $Re = 400$ (top-right), $Re = 1000$ (bottom-left) and $Re = 3200$ (bottom-right). The contour values used here are taken to be the same as those in [Ghia, Ghia, and Shin (1982)]

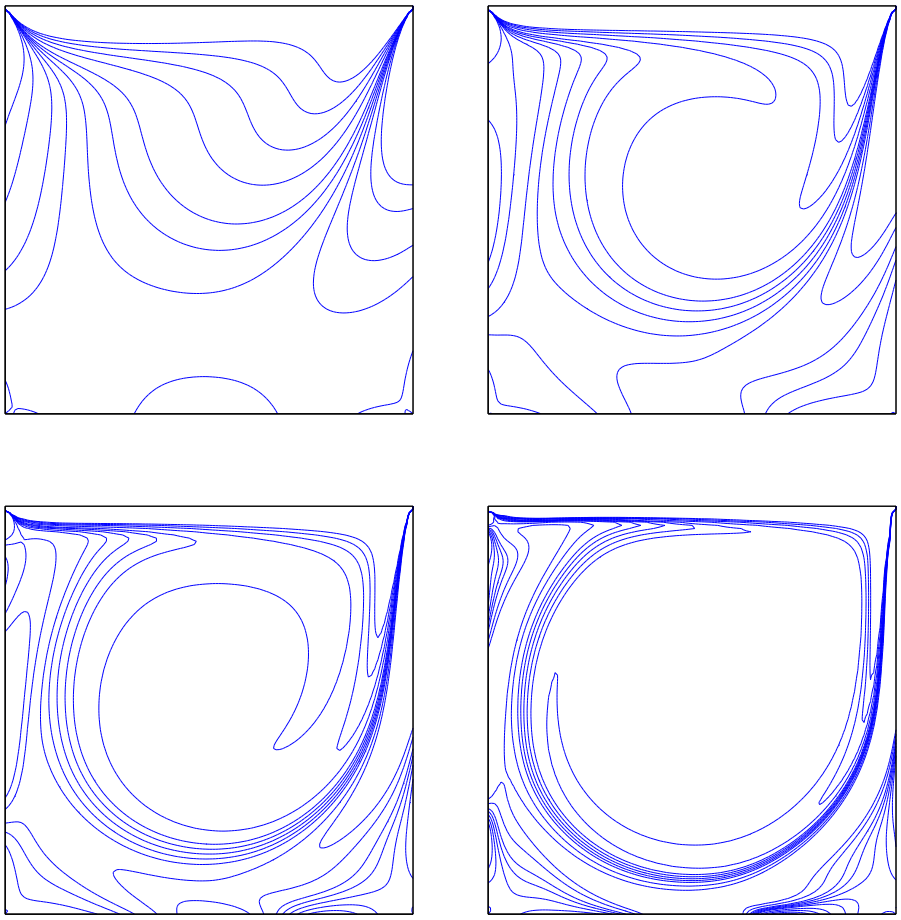

Figure 11: Example 4, Lid-driven cavity flow, 129×129: Iso-vorticity lines of the flow for $Re = 100$ (top-left), $Re = 400$ (top-right), $Re = 1000$ (bottom-left) and $Re = 3200$ (bottom-right). The contour values used here are taken to be the same as those in [Ghia, Ghia, and Shin (1982)]